Reconstruction of nonstationary sound fields based on the time domain plane wave superposition method

Xiao-Zheng Zhang
Institute of Sound and Vibration Research, Hefei University of Technology, 193 Tunxi Road, Hefei 230009, People's Republic of China

Jean-Hugh Thomas
Laboratoire d'Acoustique de l'Université du Maine (LAUM UMR-CNRS 6613), Avenue O. Messiaen, 72085 Le Mans Cedex 09, France

Chuan-Xing Bi[a)]
Institute of Sound and Vibration Research, Hefei University of Technology, 193 Tunxi Road, Hefei 230009, People's Republic of China

Jean-Claude Pascal
Laboratoire d'Acoustique de l'Université du Maine (LAUM UMR-CNRS 6613), Avenue O. Messiaen, 72085 Le Mans Cedex 09, France

(Received 18 January 2012; revised 19 July 2012; accepted 24 July 2012)

A time-domain plane wave superposition method is proposed to reconstruct nonstationary sound fields. In this method, the sound field is expressed as a superposition of time convolutions between the estimated time-wavenumber spectrum of the sound pressure on a virtual source plane and the time-domain propagation kernel at each wavenumber. By discretizing the time convolutions directly, the reconstruction can be carried out iteratively in the time domain, thus providing the advantage of continuously reconstructing time-dependent pressure signals. In the reconstruction process, the Tikhonov regularization is introduced at each time step to obtain a relevant estimate of the time-wavenumber spectrum on the virtual source plane. Because the double infinite integral of the two-dimensional spatial Fourier transform is discretized directly in the wavenumber domain in the proposed method, it does not need to perform the two-dimensional spatial fast Fourier transform that is generally used in time domain holography and real-time near-field acoustic holography, and therefore it avoids some errors associated with the two-dimensional spatial fast Fourier transform in theory and makes possible to use an irregular microphone array. The feasibility of the proposed method is demonstrated by numerical simulations and an experiment with two speakers.
 [http://dx.doi.org/10.1121/1.4746035]

PACS number(s): 43.60.Sx, 43.60.Pt, 43.60.Gk [EGW] Pages: 2427–2436

I. INTRODUCTION

Nearfield acoustic holography (NAH)[1,2] is a well-known technique for reconstructing three-dimensional sound fields based on the two-dimensional spatial fast Fourier transform (SFFT) of sound pressure data measured over a finite area. A set of methods avoiding the use of SFFT was also developed, such as statistically optimized nearfield acoustic holography (SONAH),[3–6] Helmholtz equation least-squares method (HELS),[7,8] equivalent source method (ESM),[9–14] etc. SONAH, HELS, and ESM are all based on the superposition principle: SONAH and HELS, respectively, perform the superposition of the plane wave functions and that of the spherical wave functions to fit the measured sound field data; ESM performs the superposition of the sound fields produced by a set of equivalent sources to fit the given boundary condition on the source surface or to fit the sound field data on the measurement surface.

However, SONAH and ESM are usually applied to stationary sound fields. When the signals emitted by sources are nonstationary, these two methods are unsuitable because the spatial sound fields have statistical properties that fluctuate with time. HELS can be implemented with a convolution over time kernels for studying transient sound fields.[15] Recently, transient NAH based on an interpolated time-domain ESM was also proposed to reconstruct transient acoustic fields directly in the time domain.[16] To analyze nonstationary sound fields, Hald[17] proposed a method called time domain holography (TDH). The reconstruction process of TDH can be described as follows: The frequency spectra of the pressure for each measurement point are first acquired by applying the Fourier transform to the measured time-dependent pressure signals, then for each angular frequency, the reconstruction from the measurement plane to the source plane is performed using standard NAH; finally an inverse Fourier transform yields the time-dependent pressure on the source plane. TDH is particularly well-adapted to the study of short time events due to the use of the Fourier operators to the time-dependent pressure signals. Real-time near-field acoustic holography (RT-NAH) proposed by Thomas

a)Author to whom correspondence should be addressed. Electronic mail: cxbi@hfut.edu.cn

et al.[18,19] has the advantage to continuously reconstruct time-dependent pressure signals whatever the size of the signals analyzed. It is based on a time convolution formulation in the time-wavenumber domain between the time fluctuating wavenumber spectrum and an inverse impulse response.

However, either in TDH or in RT-NAH, the two-dimensional SFFT of the measured sound pressure is employed. To reconstruct nonstationary sound fields, a time domain plane wave superposition method (TD-PWSM) is proposed in this paper. Unlike TDH and RT-NAH, TD-PWSM replaces two-dimensional SFFT with the direct discretization of double infinite integral of two-dimensional spatial Fourier transform in the wavenumber domain to avoid some limitations associated with the SFFT in theory and then expresses the sound field as a superposition of the time convolutions between the estimated time-wavenumber spectrum of the sound pressure on the virtual source plane and the time-domain propagation kernel at all wavenumbers. But similarly to RT-NAH, TD-PWSM performs the reconstruction directly in the time domain; this also provides the advantage of continuously reconstructing time-dependent pressure signals.

In Sec. II, the basic theory of TD-PWSM is outlined. The formulas of TD-PWSM are deduced in Sec. II A. Section II B describes the discretization method and an iterative reconstruction process in detail. Because the reconstruction process at each time step is ill-conditioned, the Tikhonov regularization is introduced into the reconstruction process. Sections III and IV, respectively, present a simulation and an experiment to examine the feasibility of reconstructing nonstationary sound fields by using TD-PWSM.

II. THEORY OF TD-PWSM

A. The formulas of TD-PWSM

Assume that all sources are behind the calculation plane $z = z_c$. There exist a virtual source plane $z = z_v$ in the half space $z \le z_c$ and a measurement plane $z = z_m$ with N measurement points in the half space $z > z_c$, as shown in Fig. 1.

According to the forward propagation formulation of the sound pressure in the time-wavenumber domain as shown in Refs. 20 and 21, the time-wavenumber spectrum of the pressure on the measurement plane can be expressed as the convolution of that on the virtual source plane and the impulse response function, that is

$$P(k_x, k_y, z_m, t) = P(k_x, k_y, z_v, t) * h(k_x, k_y, \Delta z_{mv}, t), \tag{1}$$

where $\Delta z_{mv} = z_m - z_v$, $h(k_x, k_y, z_m - z_v, t)$ is the impulse response function and given by

$$h(k_x, k_y, \Delta z_{mv}, t) = \delta(t - \Delta z_{mv}/c) - \Delta z_{mv}\sqrt{k_x^2 + k_y^2} \times \frac{J_1(c\sqrt{k_x^2 + k_y^2}\sqrt{t^2 - \Delta z_{mv}^2/c^2})}{\sqrt{t^2 - \Delta z_{mv}^2/c^2}} \times H(t - \Delta z_{mv}/c). \tag{2}$$

In Eq. (2), c denotes the sound velocity, $\delta(t)$ denotes the Dirac delta function, J_1 denotes the Bessel function of the first kind and order 1, and $H(t)$ denotes the Heaviside function. By applying the inverse two-dimensional spatial Fourier transform with respect to x and y to Eq. (1), it yields

$$\begin{aligned} p(x, y, z_m, t) &= \frac{1}{(2\pi)^2}\int_{-\infty}^{\infty}\int_{-\infty}^{\infty}[P(k_x, k_y, z_v, t) \\ &\quad * h(k_x, k_y, \Delta z_{mv}, t)]\, e^{-j(k_x x + k_y y)} dk_x dk_y \\ &= \frac{1}{(2\pi)^2}\int_{-\infty}^{\infty}\int_{-\infty}^{\infty} P(k_x, k_y, z_v, t) \\ &\quad * [h(k_x, k_y, \Delta z_{mv}, t) e^{-j(k_x x + k_y y)}]\, dk_x dk_y. \end{aligned} \tag{3}$$

Through setting $\mathbf{r} = (x, y)$, which represents a coordinate vector of any point in the space, and $\mathbf{K} = (k_x, k_y)$, which represents a wavenumber vector, Eq. (3) is rewritten as

$$\begin{aligned} p(\mathbf{r}, z_m, t) &= \frac{1}{(2\pi)^2}\int_{-\infty}^{\infty}\int_{-\infty}^{\infty} P(\mathbf{K}, z_v, t) \\ &\quad * [h(\mathbf{K}, \Delta z_{mv}, t) e^{-j(\mathbf{K}\cdot\mathbf{r})}]\, d\mathbf{K}. \end{aligned} \tag{4}$$

In Eq. (4), the double integral is discretized in the wavenumber domain, then $p(\mathbf{r}, z_m, t)$ is approximately given by

$$p(\mathbf{r}, z_m, t) \approx \sum_{l=1}^{L} P(\mathbf{K}_l, z_v, t) * \left[\frac{\Delta k_x \Delta k_y}{(2\pi)^2} h(\mathbf{K}_l, \Delta z_{mv}, t) e^{-j(\mathbf{K}_l\cdot\mathbf{r})}\right]. \tag{5}$$

Here, $\{\mathbf{K}_l,\ l = 1, \ldots L\}$ is the set of the sampling points in the wavenumber domain. Δk_x and Δk_y are the sampling spacing, respectively, for k_x and k_y wavenumbers. When $\Delta k_x \to 0$, $\Delta k_y \to 0$, and $L \to \infty$, the accurate value of $p(\mathbf{r}, z_m, t)$ can be obtained from Eq. (5). However, due to discrete computing, these conditions are never fulfilled. Meanwhile, because the evanescent waves corresponding to the larger wavenumbers rapidly decay with an increasing distance, the tiny contributions associated with the larger wavenumbers on the sound pressure $p(\mathbf{r}, z_m, t)$ can be neglected. Thus the almost accurate value of $p(\mathbf{r}, z_m, t)$ can be obtained by giving L, a limited number of wavenumbers. The choice of L has to ensure that the sampling area in the wavenumber

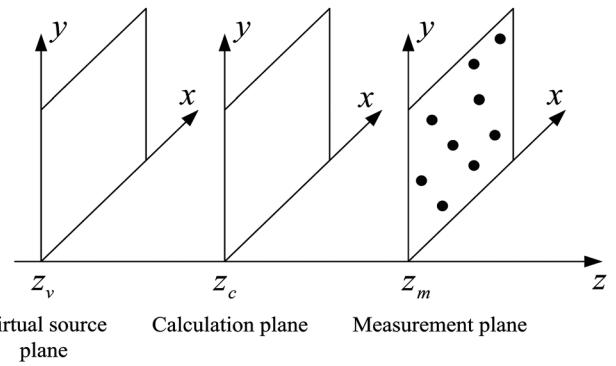

FIG. 1. Geometry of the virtual source plane, the calculation plane, and the measurement plane.

domain covers all propagating waves and those evanescent waves that have significant amplitude in the measurement region.[5] Defining the time-domain propagation kernel between the sound pressure on the measurement plane $p(\mathbf{r}, z_m, t)$ and the time-wavenumber spectrum of the sound pressure on the virtual source plane $P(\mathbf{K}_l, z_v, t)$ as

$$\psi(\mathbf{K}_l, \mathbf{r}, \Delta z_{mv}, t) = \frac{\Delta k_x \Delta k_y}{(2\pi)^2} h(\mathbf{K}_l, \Delta z_{mv}, t) e^{-j(\mathbf{K}_l \cdot \mathbf{r})}, \tag{6}$$

Eq. (5) can be rewritten as

$$p(\mathbf{r}, z_m, t) = \sum_{l=1}^{L} P(\mathbf{K}_l, z_v, t) * \psi(\mathbf{K}_l, \mathbf{r}, \Delta z_{mv}, t). \tag{7}$$

Similarly the time-dependent spatial sound field on the calculation plane $z = z_c$ is

$$p(\mathbf{r}, z_c, t) = \sum_{l=1}^{L} P(\mathbf{K}_l, z_v, t) * \psi(\mathbf{K}_l, \mathbf{r}, \Delta z_{cv}, t), \tag{8}$$

where $\Delta z_{cv} = z_c - z_v$. Equations (7) and (8) constitute the basic formulas of the TD-PWSM that describe the time-dependent sound pressure radiated by the actual sources as a superposition of the time convolutions between the time-wavenumber spectrum of the sound pressure on the virtual source plane and the time-domain propagation kernel at each wavenumbers. If the time-wavenumber spectrum $P(\mathbf{K}_l, z_v, t)$ in Eq. (7) can be estimated properly by fitting the measured sound pressure $p(\mathbf{r}, z_m, t)$ and then is substituted to Eq. (8), the time-dependent spatial sound field on the calculation plane $p(\mathbf{r}, z_c, t)$ would be directly obtained.

The aforementioned derivation process demonstrates the two-dimensional SFFT of the measured sound pressure is not used in the reconstruction process. Obviously, the double infinite integral of the two-dimensional spatial Fourier transform is discretized directly in the wavenumber domain. In TDH and RT-NAH, the use of SFFT leads to confine k_x and k_y to $[-\pi/a, \pi/a]$ where a is the sample spacing of the spatial function, and the wavenumber resolutions Δk_x and Δk_y are always equal to $2\pi/W$ where W is the measurement aperture in the x direction or in the y direction. In TD-PWSM, the direct discretization of the integral brings the freedom of extending the scope of k_x and k_y and narrowing the width of Δk_x and Δk_y. The extension provides abundant evanescent wave information in the reconstruction results, and the narrowing of Δk_x and Δk_y implies that the aperture in the space domain is enlarged; this weakens the effect of wrap-around errors on the reconstruction results. Moreover, similarly to RT-NAH, the TD-PWSM performs the reconstruction directly in the time domain, which also provides the ability of continuously reconstructing time-dependent pressure signals. The following section will describe this ability in detail.

B. The discretization and reconstruction process

To implement Eqs. (7) and (8), the discrete time variable t_i such as

$$t_i = (i-1)\Delta t, \quad i = 1, 2, \cdots I, \tag{9}$$

is used where Δt is the sampling period. According to Eqs. (2) and (6), the time-domain propagation kernel $\psi(\mathbf{K}_l, \mathbf{r}, \Delta z_{mv}, t)$ is equal to zero for $t < \tau$ caused by the fact that the impulse response function $h(k_x, k_y, \Delta z_{mv}, t)$ equals to zero for $t < \tau$. $\tau = \Delta z_{mv}/c$ corresponds to the time needed for the waves to propagate from the virtual source plane to the measurement plane. Consider that t_k is the nearest time step more than or equal to τ. According to the discrete convolution formula, at time step t_k, the spatial sound pressure on the measurement plane $z = z_m$ is

$$p(\mathbf{r}, z_m, t_k) = \sum_{l=1}^{L} P(\mathbf{K}_l, z_v, t_1) \times \psi(\mathbf{K}_l, \mathbf{r}, \Delta z_{mv}, t_k) \times \Delta t. \tag{10}$$

Here for the sake of simplicity, Δt is omitted in the following formulas. The matrix formulation

$$\mathbf{p}_m^k = \mathbf{\Psi}_m^k \mathbf{P}^1, \tag{11}$$

where

$$\mathbf{p}_m^k = [\, p(\mathbf{r}_1, z_m, t_k) \quad p(\mathbf{r}_2, z_m, t_k) \quad \cdots \quad p(\mathbf{r}_N, z_m, t_k) \,]^T, \tag{12}$$

$$\mathbf{P}^1 = [\, P(\mathbf{K}_1, z_v, t_1) \quad P(\mathbf{K}_2, z_v, t_1) \quad \cdots \quad P(\mathbf{K}_L, z_v, t_1) \,]^T, \tag{13}$$

$$\mathbf{\Psi}_m^k = \begin{bmatrix} \psi(\mathbf{K}_1, \mathbf{r}_1, \Delta z_{mv}, t_k) & \psi(\mathbf{K}_2, \mathbf{r}_1, \Delta z_{mv}, t_k) & \cdots & \psi(\mathbf{K}_L, \mathbf{r}_1, \Delta z_{mv}, t_k) \\ \psi(\mathbf{K}_1, \mathbf{r}_2, \Delta z_{mv}, t_k) & \psi(\mathbf{K}_2, \mathbf{r}_2, \Delta z_{mv}, t_k) & \cdots & \psi(\mathbf{K}_L, \mathbf{r}_2, \Delta z_{mv}, t_k) \\ \vdots & \vdots & \vdots & \vdots \\ \psi(\mathbf{K}_1, \mathbf{r}_N, \Delta z_{mv}, t_k) & \psi(\mathbf{K}_2, \mathbf{r}_N, \Delta z_{mv}, t_k) & \cdots & \psi(\mathbf{K}_L, \mathbf{r}_N, \Delta z_{mv}, t_k) \end{bmatrix}, \tag{14}$$

has the advantage to describe Eq. (10) for N measurement points of coordinate $\mathbf{r}_n$ $(n = 1, \ldots N)$. Note that $\mathbf{\Psi}_m^k$ is a $N \times L$ matrix. If the number of measurement points N is larger than the number of discrete wavenumbers L, the wavenumber spectrum on the virtual source plane at time t_1 is provided using the left pseudo-inverse of matrix $\mathbf{\Psi}_m^k$. The least-squares solution of Eq. (11) is then expressed as

$$\tilde{\mathbf{P}}^1 = (\boldsymbol{\Psi}_m^{k\ H}\boldsymbol{\Psi}_m^k)^{-1}\boldsymbol{\Psi}_m^{k\ H}\mathbf{p}_m^k, \tag{15}$$

where the symbol H represents the Hermitian transpose. Although the condition $N \geq L$ ensures the uniqueness of the solution to the inverse problem, it leads to the requirement of a large number of microphones for obtaining a space map with the sufficient resolution. In practice, it is costly and difficult to meet this requirement. Therefore it is more realistic to consider the number of measurement points N is smaller than the number of discrete wavenumbers L. Although Eq. (11) is under-determined when $N < L$ and has infinitely many solutions, its smallest two-norm solution can be obtained using the right pseudo-inverse of matrix $\boldsymbol{\Psi}_m^k$, which is the standard way to deal with under-determined cases in linear algebra.[22] The smallest two-norm solution of Eq. (11) is expressed as

$$\tilde{\mathbf{P}}^1 = [\boldsymbol{\Psi}_m^k]^{+R}\mathbf{p}_m^k, \tag{16}$$

where $[\boldsymbol{\Psi}_m^k]^{+R}$ represents the right pseudo-inverse of matrix $\boldsymbol{\Psi}_m^k$ and is given by

$$[\boldsymbol{\Psi}_m^k]^{+R} = \boldsymbol{\Psi}_m^{k\ H}(\boldsymbol{\Psi}_m^k\boldsymbol{\Psi}_m^{k\ H})^{-1}. \tag{17}$$

Once the smallest two-norm solution $\tilde{\mathbf{P}}^1$ is solved, the pressure at any point $\mathbf{r}'$ on the calculation surface at the first time step t_1 can be deduced as

$$\tilde{p}(\mathbf{r}', z_c, t_1) = \boldsymbol{\Psi}_c^1\tilde{\mathbf{P}}^1, \tag{18}$$

where

$$\boldsymbol{\Psi}_c^1 = [\psi(\mathbf{K}_1, \mathbf{r}', \Delta z_{cv}, t_1) \quad \psi(\mathbf{K}_2, \mathbf{r}', \Delta z_{cv}, t_1) \ \cdots \ \psi(\mathbf{K}_L, \mathbf{r}', \Delta z_{cv}, t_1)]. \tag{19}$$

According to the discrete convolution formula, at time step t_{k+1}, the spatial sound pressure on the measurement plane becomes

$$p(\mathbf{r}, z_m, t_{k+1}) = \sum_{l=1}^{L} P(\mathbf{K}_l, z_v, t_2) \times \psi(\mathbf{K}_l, \mathbf{r}, \Delta z_{mv}, t_k) + P(\mathbf{K}_l, z_v, t_1) \times \psi(\mathbf{K}_l, \mathbf{r}, \Delta z_{mv}, t_{k+1}). \tag{20}$$

Equation (20) can be described in the matrix form as

$$\mathbf{p}_m^{k+1} = \boldsymbol{\Psi}_m^k\mathbf{P}^2 + \boldsymbol{\Psi}_m^{k+1}\mathbf{P}^1, \tag{21}$$

where

$$\mathbf{p}_m^{k+1} = [p(\mathbf{r}_1, z_m, t_{k+1}) \quad p(\mathbf{r}_2, z_m, t_{k+1}) \ \cdots \ p(\mathbf{r}_N, z_m, t_{k+1})]^T, \tag{22}$$

$$\boldsymbol{\Psi}_m^{k+1} = \begin{bmatrix} \psi(\mathbf{K}_1, \mathbf{r}_1, \Delta z_{mv}, t_{k+1}) & \psi(\mathbf{K}_2, \mathbf{r}_1, \Delta z_{mv}, t_{k+1}) & \cdots & \psi(\mathbf{K}_L, \mathbf{r}_1, \Delta z_{mv}, t_{k+1}) \\ \psi(\mathbf{K}_1, \mathbf{r}_2, \Delta z_{mv}, t_{k+1}) & \psi(\mathbf{K}_2, \mathbf{r}_2, \Delta z_{mv}, t_{k+1}) & \cdots & \psi(\mathbf{K}_L, \mathbf{r}_2, \Delta z_{mv}, t_{k+1}) \\ \vdots & \vdots & \vdots & \vdots \\ \psi(\mathbf{K}_1, \mathbf{r}_N, \Delta z_{mv}, t_{k+1}) & \psi(\mathbf{K}_2, \mathbf{r}_N, \Delta z_{mv}, t_{k+1}) & \cdots & \psi(\mathbf{K}_L, \mathbf{r}_N, \Delta z_{mv}, t_{k+1}) \end{bmatrix}. \tag{23}$$

In Eq. (21), $\boldsymbol{\Psi}_m^k$, $\boldsymbol{\Psi}_m^{k+1}$, and $\mathbf{p}_m^{k+1}$ are known quantities, and $\mathbf{P}^1$ is replaced with $\tilde{\mathbf{P}}^1$. Similarly, using the right pseudo-inverse of matrix $\boldsymbol{\Psi}_m^k$, the smallest two-norm solution of Eq. (21) is expressed as

$$\tilde{\mathbf{P}}^2 = [\boldsymbol{\Psi}_m^k]^{+R}(\mathbf{p}_m^{k+1} - \boldsymbol{\Psi}_m^{k+1}\tilde{\mathbf{P}}^1). \tag{24}$$

Once the smallest two-norm solution $\tilde{\mathbf{P}}^2$ is solved, the pressure at any point $\mathbf{r}'$ on the calculation plane at the second time step t_2 can be deduced as

$$\tilde{p}(\mathbf{r}', z_c, t_2) = \boldsymbol{\Psi}_c^1\tilde{\mathbf{P}}^2 + \boldsymbol{\Psi}_c^2\tilde{\mathbf{P}}^1, \tag{25}$$

where

$$\boldsymbol{\Psi}_c^2 = [\psi(\mathbf{K}_1, \mathbf{r}', \Delta z_{cv}, t_2) \quad \psi(\mathbf{K}_2, \mathbf{r}', \Delta z_{cv}, t_2) \ \cdots \ \psi(\mathbf{K}_L, \mathbf{r}', \Delta z_{cv}, t_2)]. \tag{26}$$

And so forth, the solution at the ith time step t_i ($i = 3, 4, \cdots I - k + 1$) is given by

$$\tilde{\mathbf{P}}^i = [\boldsymbol{\Psi}_m^k]^{+R}(\mathbf{p}_m^{i+k-1} - \boldsymbol{\Psi}_m^{k+1}\tilde{\mathbf{P}}^{i-1} - \boldsymbol{\Psi}_m^{k+2}\tilde{\mathbf{P}}^{i-2} - \cdots - \boldsymbol{\Psi}_m^{i+k-1}\tilde{\mathbf{P}}^1). \tag{27}$$

Thus the pressure is obtained at any point $\mathbf{r}'$ on the calculation surface at the ith time step t_i

$$\tilde{p}(\mathbf{r}', z_c, t_i) = \boldsymbol{\Psi}_c^1\tilde{\mathbf{P}}^i + \boldsymbol{\Psi}_c^2\tilde{\mathbf{P}}^{i-1} + \cdots + \boldsymbol{\Psi}_c^i\tilde{\mathbf{P}}^1, \tag{28}$$

where

$$\boldsymbol{\Psi}_c^i = [\psi(\mathbf{K}_1, \mathbf{r}', \Delta z_{cv}, t_i) \quad \psi(\mathbf{K}_2, \mathbf{r}', \Delta z_{cv}, t_i) \ \cdots \ \psi(\mathbf{K}_L, \mathbf{r}', \Delta z_{cv}, t_i)]. \tag{29}$$

In Eqs. (16), (24), and (27), the direct use of the right pseudo-inverse of matrix $\boldsymbol{\Psi}_m^k$ leads to an inappropriate solution because the inversion is often ill-conditioned. Furthermore the above-mentioned iterative algorithm causes the increase of calculation errors with time. To obtain an appropriate solution and suppress the increase of calculation

errors, the Tikhonov regularization[23] is implemented at each time step. Then the smallest two-norm solution at the ith time step t_i ($i = 1, 2, \cdots I-k+1$) becomes

$$\tilde{\mathbf{P}}_{\lambda}^{i} = [\boldsymbol{\Psi}_m^k]_{\lambda}^{+R}(\mathbf{p}_m^{i+k-1} - \boldsymbol{\Psi}_m^{k+1}\tilde{\mathbf{P}}^{i-1} - \boldsymbol{\Psi}_m^{k+2}\tilde{\mathbf{P}}^{i-2} - \cdots - \boldsymbol{\Psi}_m^{i+k-1}\tilde{\mathbf{P}}^{1}), \tag{30}$$

where $\tilde{\mathbf{P}}_{\lambda}^{i}$ denotes the regularized solution, and

$$[\boldsymbol{\Psi}_m^k]_{\lambda}^{+R} = \boldsymbol{\Psi}_m^{k\,H}(\boldsymbol{\Psi}_m^k \boldsymbol{\Psi}_m^{k\,H} + \lambda \mathbf{I})^{-1}. \tag{31}$$

The regularization parameter λ is estimated by the generalized cross validation (GCV),[24] which consists of minimizing the function $J(\lambda)$ defined by

$$J(\lambda) = \frac{\|\boldsymbol{\Psi}_m^k \tilde{\mathbf{P}}_{\lambda}^{i} - \mathbf{B}\|^2}{[Tr(\mathbf{I} - \boldsymbol{\Psi}_m^k [\boldsymbol{\Psi}_m^k]_{\lambda}^{+R})]^2}, \tag{32}$$

where

$$\mathbf{B} = \mathbf{p}_m^{i+k-1} - \boldsymbol{\Psi}_m^{k+1}\tilde{\mathbf{P}}^{i-1} - \boldsymbol{\Psi}_m^{k+2}\tilde{\mathbf{P}}^{i-2} - \cdots - \boldsymbol{\Psi}_m^{i+k-1}\tilde{\mathbf{P}}^{1}. \tag{33}$$

Because the matrix $\mathbf{B}$ is different at each time step, the regularization parameter selected by Eq. (32) also changes with time step. Currently, we have not found the significant trend and regular pattern from the evolution of the regularization parameter, and it is not sure that the regularization parameter values returned from the GCV are always appropriate. Nevertheless in the following, the relevance of the results provided by the TD-PWSM method based on this regularization is shown.

III. NUMERICAL SIMULATIONS

The setup of the numerical simulations is shown in Fig. 2. The sources are composed of two monopoles the positions of which are $M_1(0.09\,\text{m}, 0.27\,\text{m}, 0\,\text{m})$ and $M_2(0.45\,\text{m}, 0.27\,\text{m}, 0\,\text{m})$. M_1 generates a nonstationary signal with a linear frequency modulation in the [200, 1800] Hz band and a Gaussian amplitude modulation. M_2 radiates another nonstationary signal–Morlet wavelet defined by

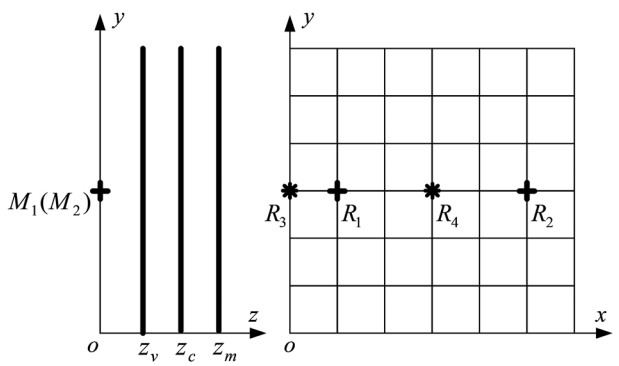

FIG. 2. Geometric description of the virtual source plane, the calculation plane, and the measurement plane. Points R_1 and R_2 marked with + stand for the points facing the source M_1 and the source M_2, respectively. Points R_3 and R_4 marked with * stand for the points not facing sources.

$$s(t) = \cos(2\pi f_0 t)e^{-t^2/2}, \tag{34}$$

with $f_0 = 800\,\text{Hz}$. The measurement plane located at $z_m = 0.13\,\text{m}$ provides 7×7 measurement points, and the spacing of measurement points in both x and y directions is set to $a = 0.09\,\text{m}$. The calculation plane is located at $z_c = 0.09\,\text{m}$, and the virtual source plane is located at $z_v = 0.06\,\text{m}$. The emitted signals are sampled at a frequency $f_e = 34\,400\,\text{Hz}$ providing 256 samples. According to the Nyquist theorem, the wavenumber domain sampling area is given as $[-\pi/a, \pi/a]$. This sampling area is supposed to cover all propagating waves and those evanescent waves that have significant amplitude in the measurement region. In theory, the wavenumber domain sampling spacing should be equal to zero for realizing all wavenumber sampling in the given sampling area. However, due to discrete computing, the wavenumber domain sampling spacing can just take a value more than zero. It is certain that the smaller is this taken value, the more accurate is the approximation in Eq. (5), but the smaller value will lead to the bigger computation loads. Basing on the comprehensive consideration of the calculation precision and the computational efficiency, the wavenumber domain sampling spacing is given as $\pi/(18a)$. A Gaussian white noise with a signal-to-noise ratio (SNR) of 20 dB is also added to the simulated signals.

For the sake of assessing the relevance of the proposed method in the time domain, four space points on the calculation plane are chosen, and their positions are $R_1(0.09\,\text{m}, 0.27\,\text{m}, 0.09\,\text{m})$, $R_2(0.45\,\text{m}, 0.27\,\text{m}, 0.09\,\text{m})$, $R_3(0\,\text{m}, 0.27\,\text{m}, 0.09\,\text{m})$, and $R_4(0.27\,\text{m}, 0.27\,\text{m}, 0.09\,\text{m})$. As shown in Fig. 2, R_1 and R_2 are facing the source M_1 and the source M_2, respectively, R_3 is located at the edge of the calculation plane, and R_4 is located in the center of the calculation plane. Figure 3 shows the comparisons between the calculated pressure and the theoretical pressure at these points in the time domain. It is demonstrated that the calculated results provide accurate phases at all four points and a lower magnitude than that of the theoretical pressure at R_3.

To comment more objectively about the results calculated in the time domain, two error indicators T_1 and T_2 are computed for a point (x_i, y_j) on the calculation plane. They are defined by

$$T_1(x_i, y_j) = \frac{<p_t(x_i, y_j, z_c, t)p_c(x_i, y_j, z_c, t)>_t}{\sqrt{<p_t^2(x_i, y_j, z_c, t)>_t < p_c^2(x_i, y_j, z_c, t)>_t}}, \tag{35}$$

$$T_2(x_i, y_j) = \frac{|p_t^{rms}(x_i, y_j, z_c) - p_c^{rms}(x_i, y_j, z_c)|}{p_t^{rms}(x_i, y_j, z_c)}, \tag{36}$$

where $p_t^{rms}(x_i, y_j, z_c)$ and $p_c^{rms}(x_i, y_j, z_c)$ are the root mean square pressure values given by

$$p_t^{rms}(x_i, y_j, z_c) = \sqrt{<p_t^2(x_i, y_j, z_c, t)>_t}, \tag{37}$$

$$p_c^{rms}(x_i, y_j, z_c) = \sqrt{<p_c^2(x_i, y_j, z_c, t)>_t}. \tag{38}$$

$<>_t$ denotes the time averaged value. $p_t(x_i, y_j, z_c, t)$ is the theoretical time-dependent pressure, and $p_c(x_i, y_j, z_c, t)$ is

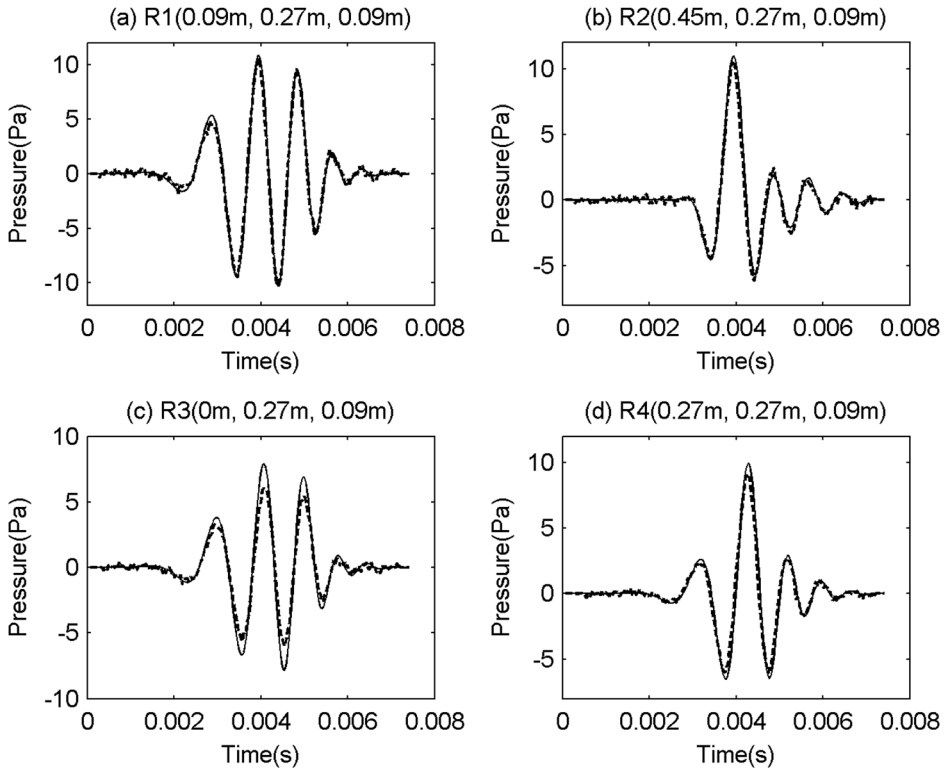

FIG. 3. Comparison between the time-dependent pressure signals on the calculation plane in points R_1 (a), R_2 (b), R_3 (c), and R_4 (d): The theoretical pressure (solid line) and the calculated pressure (dashed line).

the calculated time-dependent pressure. T_1 and T_2 are sensitive to the phase differences and the magnitude differences between $p_t(x_i, y_j, z_c, t)$ and $p_c(x_i, y_j, z_c, t)$, respectively. Phase accuracy gives T_1 in the neighborhood of 1, and magnitude accuracy gives T_2 near 0. The values of both indicators T_1 and T_2 are computed for each point on the calculation plane. The map of indicator T_1 with the 0.95 contour line is shown in Fig. 4(a), and the map of indicator T_2 with the 0.1 contour line is shown in Fig. 4(b). In Fig. 4(a), the values of indicator T_1 at all points are greater than 0.95, which indicates that the phase of the calculated pressure matches well with that of the theoretical pressure. Figure 4(b) shows that the values of indicator T_2 are below 0.1 for most space points. The values of indicator T_1 at marked points $R_1(+)$, $R_2(+)$, $R_3(*)$, and $R_4(*)$ are 0.996, 0.990, 0.994, and 0.990, respectively. The values of indicator T_2 at marked points $R_1(+)$, $R_2(+)$, $R_3(*)$, and $R_4(*)$ are 0.041, 0.058, 0.214, and 0.093, respectively.

Similarly, to highlight the relevance of the proposed method in the space domain, two time instants ($t_{119} = 3.4$ ms and $t_{152} = 4.4$ ms) are chosen. Figures 5(a) and 5(c) show, respectively, the theoretical spatial pressure field and the calculated spatial pressure field at $t_{119} = 3.4$ ms where the source M_1 radiates with a high level and M_2 with a low level. Figures 5(b) and 5(d) show the same spatial pressure fields but at $t_{152} = 4.4$ ms where the acoustic field is dominated by the acoustic signals radiated by sources M_1 and M_2. From the comparison of the theoretical spatial pressure field

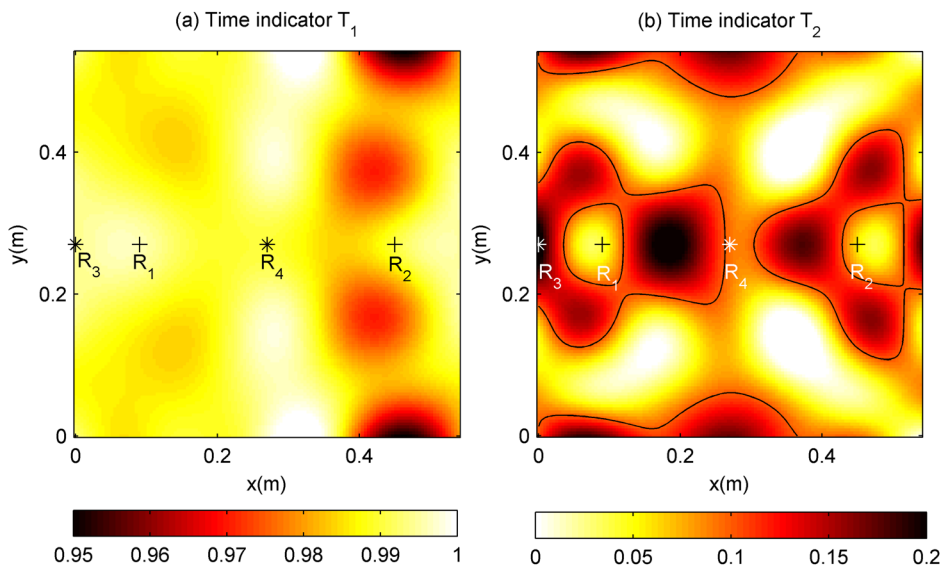

FIG. 4. (Color online) Spatial maps for indicator T_1 (a) with a contour line at the value 0.95 and for indicator T_2 (b) with a contour line at the value 0.1. The points $R_1(+)$, $R_2(+)$, $R_3(*)$, and $R_4(*)$ are marked.

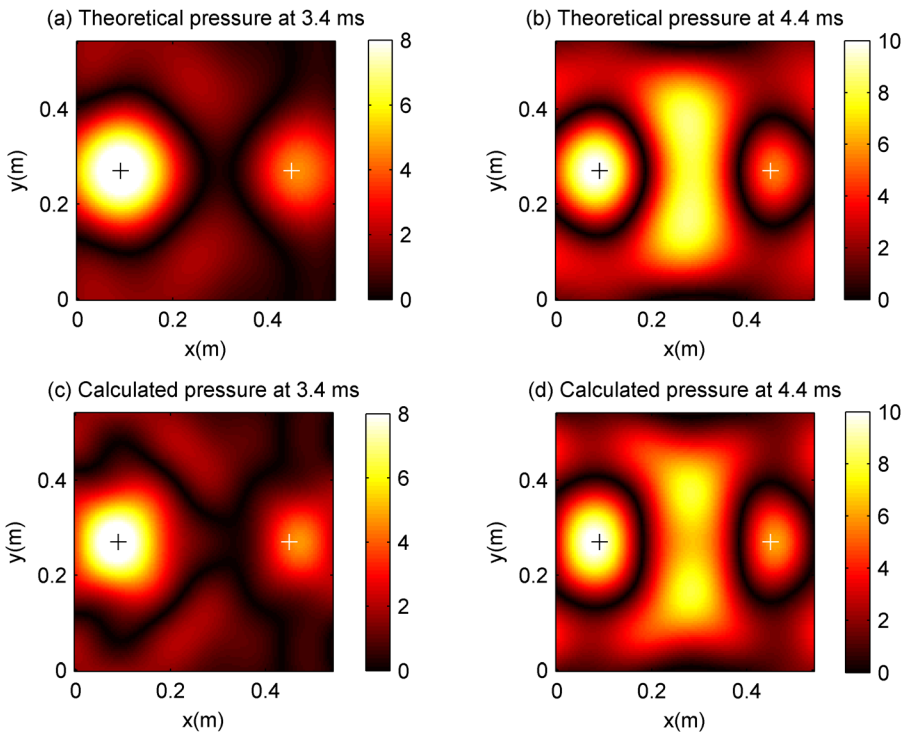

FIG. 5. (Color online) Theoretical spatial pressure field at $t_{119} = 3.4$ ms (a) and at $t_{152} = 4.4$ ms (b) versus calculated spatial pressure field at $t_{119} = 3.4$ ms (c) and at $t_{152} = 4.4$ ms (d). The left marked location is facing the source M_1, and the right marked location is facing the source M_2.

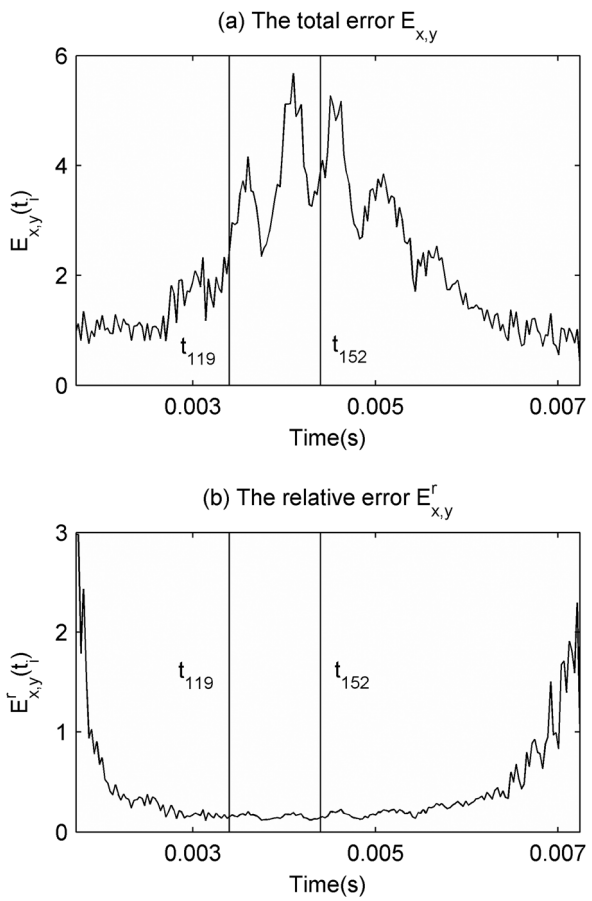

FIG. 6. Simulated results: time evolutions of the total error (a) and the relative error (b). The vertical lines indicate the time instants chosen at $t_{119} = 3.4$ ms and at $t_{152} = 4.4$ ms.

and the calculated spatial pressure field, it is demonstrated that the proposed method provides a means of visualizing the spatial pressure field when the sound field fluctuates with time.

To evaluate the quality of the results calculated in the space domain, two error criteria are introduced. One is the total error criterion, defined by

$$E_{x,y}(t_i) = \sqrt{<(p_c(x,y,t_i) - p_t(x,y,t_i))^2>_s}, \tag{39}$$

which evaluates the difference between the calculated pressure $p_c(x,y,t_i)$ and the theoretical pressure $p_t(x,y,t_i)$ at a given time t_i, and $<>_s$ denotes the spatial averaged value. The other is the relative spatial error criterion, defined by

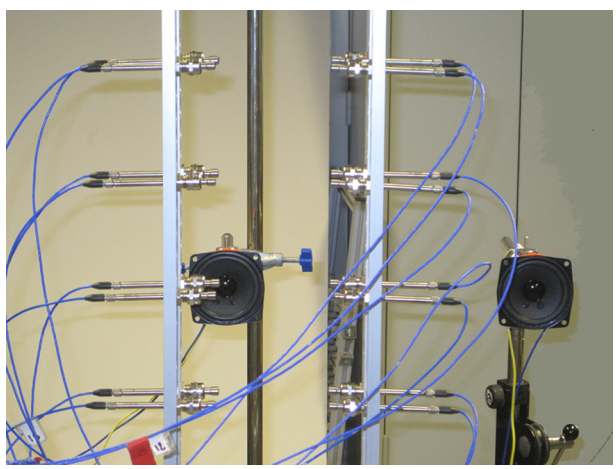

FIG. 7. (Color online) Experimental setup with two loudspeakers and a double-layer microphone array.

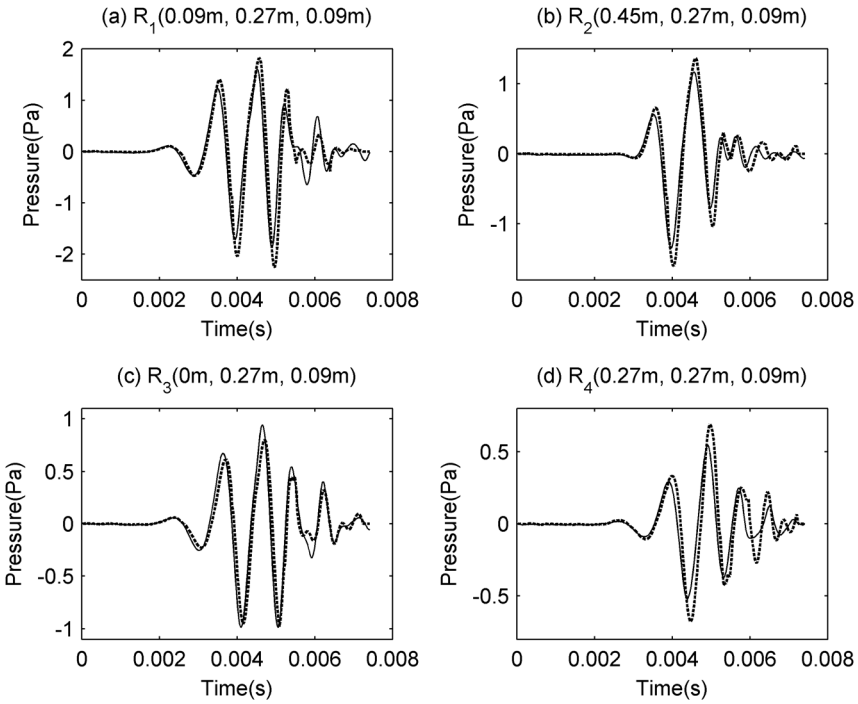

FIG. 8. Comparison between the time-dependent pressure signals on the calculation plane at points R_1 (a), R_2 (b), R_3 (c), and R_4 (d): The measured pressure (solid line) and the calculated pressure (dashed line).

$$E^r_{x,y}(t_i) = \frac{\sqrt{<(p_c(x,y,t_i) - p_t(x,y,t_i))^2>_s}}{\sqrt{<p_t^2(x,y,t_i)>_s}}, \tag{40}$$

which corresponds to the root mean square error between the calculated pressure $p_c(x,y,t_i)$ and the theoretical pressure $p_t(x,y,t_i)$ at a given time t_i and is suitable to quantify the quality of the reconstruction. The time evolutions of these two errors are shown in Fig. 6 from which it can be seen that at most time instants the values of the relative error are smaller than 0.5. High values of the error are obtained at the edges of the signal due to the fact that the theoretical pressure field supplies the denominator of Eq. (40) with very low values at these time instants. The values of the relative error at $t_{119} = 3.4$ ms and at $t_{152} = 4.4$ ms are 0.178 and 0.143, respectively.

IV. EXPERIMENT

To examine the feasibility of reconstructing nonstationary sound fields based on TD-PWSM, an experiment is carried out. The experimental setup is shown in Fig. 7.

Two loudspeakers are chosen as sources. The signals generated by these two sources are very similar to those used in the simulation case. These signals are also recorded at a sampling frequency $f_e = 34\,400$ Hz providing 256 samples.

In addition, the experiment provides the same locations for the sources and the measurement planes as those in the simulation case. A double-layer microphone array with an interval of 0.04 m, shown in Fig. 7, is used to measure simultaneously the pressure fields on both the measurement plane and the calculation plane. Each layer provides 2×4 microphones equally spaced every 0.09 m. For each measurement the array is moved, both sources are synchronized and

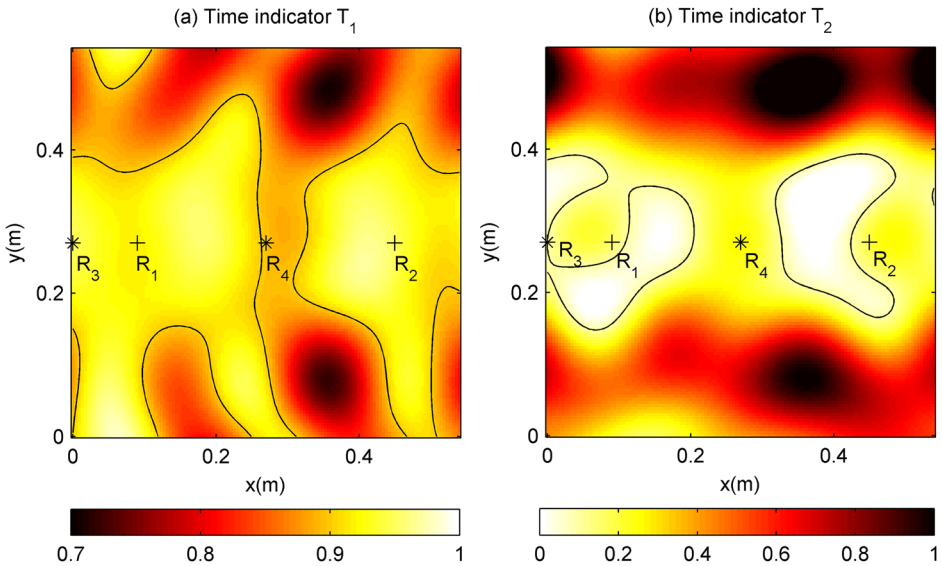

FIG. 9. (Color online) Spatial maps for indicator T_1 (a) with a contour line at the value 0.9 and for indicator T_2 (b) with a contour line at the value 0.1. The points $R_1(+)$, $R_2(+)$, $R_3(*)$, and $R_4(*)$ are marked.

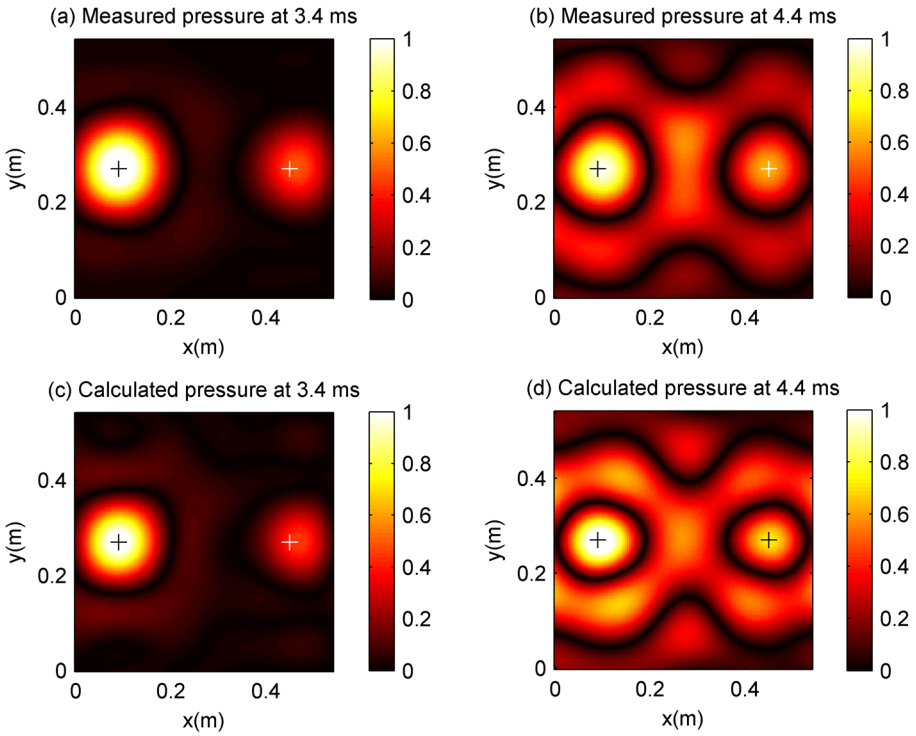

FIG. 10. (Color online) Measured spatial pressure field at $t_{119} = 3.4$ ms (a) and at $t_{152} = 4.4$ ms (b) versus calculated spatial pressure field at $t_{119} = 3.4$ ms (c) and at $t_{152} = 4.4$ ms (d).

generate exactly the same signals to simulate the simultaneous sound field acquisition on a large area composed of 7×7 measurement points providing an overall scan area of $0.54 \times 0.54\,\mathrm{m}^2$.

In the reconstruction process, the distance between the virtual source plane and the measurement plane, the wavenumber domain sampling area and the wavenumber domain sampling spacing are all the same as those selected in the simulation case.

Four space points, with the same locations as those in the simulation case, are chosen to show the results in the time domain from TD-PWSM. Figure 8 shows the comparisons between the calculated pressure and the measured pressure at these points in the time domain. Although the calculated results do not provide very accurate phases and magnitudes, especially as shown in Fig. 8(d), they at least demonstrate that TD-PWSM has the ability to reconstruct nonstationary signals in the time domain.

Indicators T_1 and T_2 are also computed for each location facing the microphone positions. The map of indicator T_1 with the 0.9 contour line is shown in Fig. 9(a), and the map of indicator T_2 with the 0.1 contour line is shown in Fig. 9(b). Figure 9 indicates that the good reconstruction results are obtained mainly in the area around two sources, and the worse reconstruction results appear in the edge of the calculation plane where all the measurement errors such as the noise from microphones, the reflection from the wall, and the scattering from the support beams become more significant. The values of indicator T_1 at marked points $R_1(+)$, $R_2(+)$, $R_3(*)$, and $R_4(*)$ are 0.918, 0.949, 0.947, and 0.895, respectively. The values of indicator T_2 at marked points $R_1(+)$, $R_2(+)$, $R_3(*)$, and $R_4(*)$ are 0.155, 0.198, 0.101, and 0.261, respectively.

The reconstruction results in the space domain are studied for the same time instants ($t_{119} = 3.4$ ms and

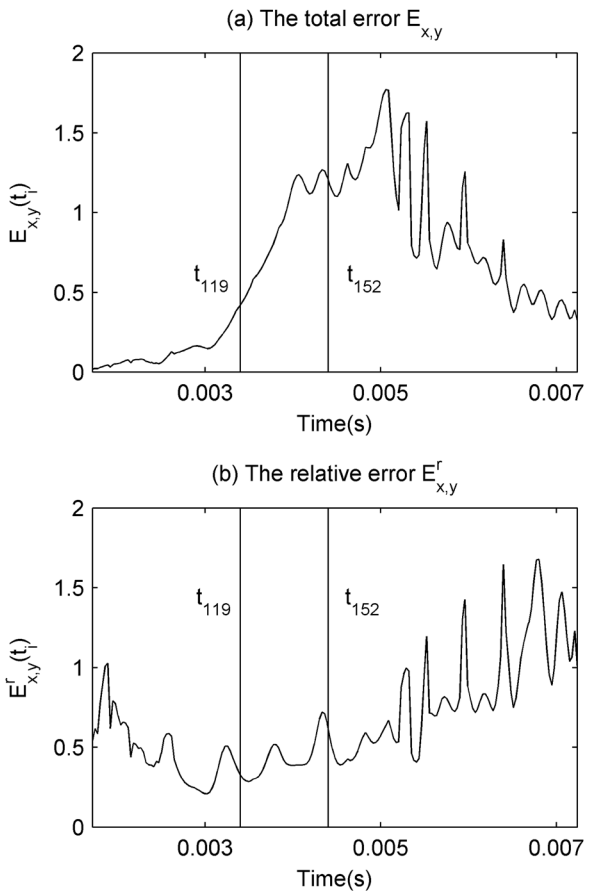

FIG. 11. Experimental results: ticme evolutions of the total error (a) and the relative error (b). The vertical lines indicate the time instants chosen at $t_{119} = 3.4$ ms and at $t_{152} = 4.4$ ms.

$t_{152} = 4.4$ ms) as in the simulation case. Figures 10(a) and 10(c), respectively, show the measured pressure and the calculated pressure at $t_{119} = 3.4$ ms. Figures 10(b) and 10(d) show the same sound fields but at $t_{152} = 4.4$ ms. Obviously, the proposed TD-PWSM seems effective to reconstruct spatial pressure fields.

The total error and the relative error defined in Eq. (39) and Eq. (40) are calculated for each time t_i. Their time evolutions are shown in Fig. 11, which highlights a somewhat similar trend as that in Fig. 6 but with less accurate values. The values of the relative error at $t_{119} = 3.4$ ms and $t_{152} = 4.4$ ms are 0.302, 0.647, respectively.

Owing to the effects of measurement errors, the experimental results are not as good as those in the simulation case, but they really demonstrate the feasibility of reconstructing nonstationary sound fields by using TD-PWSM.

V. CONCLUSIONS

A time domain plane wave superposition method was proposed to reconstruct the nonstationary sound fields. This method performs the reconstruction by replacing the two-dimensional SFFT that is generally used in TDH and RT-NAH with the direct discretization of double infinite integral in the wavenumber domain, theoretically avoiding some limitations associated with the SFFT. It also gave an iterative reconstruction process in the time domain, thus providing the ability of continuously reconstructing time-dependent pressure signals. Numerical simulations and an experiment have demonstrated that it is feasible to reconstruct the nonstationary sound fields via TD-PWSM. Due to the use of the Tikhonov regularization at each time step, the computation time required by the TD-PWSM is longer than those by TDH and RT-NAH, but this weakness does not prevent the TD-PWSM from being used in a personal computer when the signal length in the time domain is not too long. In fact, the microphone array employed by TD-PWSM could be irregular, such as cross array, circular array, random array, etc. However, the problem of which kind of array can be used to obtain the best reconstruction results is still under investigation. In addition, some parameters influencing the reconstruction results should be also investigated in future, such as the distance between the measurement plane and the virtual source plane, the distance between the calculation plane and the virtual source plane, and the regularization parameter, etc.

ACKNOWLEDGMENTS

This work was supported by National Natural Science Foundation of China (Grant Nos. 10974040 and 51105126), the Program for New Century Excellent Talents in University (Grant No. NCET-08-0767), and the Research Fund for the Doctoral Program of Higher Education (Grant No. 20100111110007). The authors would like to thank Julien Nicolas from the Ecole Nationale d'Ingénieurs du Mans (ENSIM) for his contribution to the building of the double-layer array.

[1] J. D. Maynard, E. G. Williams, and Y. Lee, "Nearfield acoustic holography. I. Theory of generalized holography and development of NAH," J. Acoust. Soc. Am. **78**(4), 1395–1413 (1985).
[2] J. D. Maynard and E. G. Williams, "Nearfield acoustic holography (NAH). II. Holographic reconstruction algorithms and computer implementation," J. Acoust. Soc. Am. **81**(5), 1307–1322 (1987).
[3] R. Steiner and J. Hald, "Near-field acoustical holography without the errors and limitations caused by the use of spatial DFT," Int. J. Acoust. Vib. **6**, 83–89 (2001).
[4] J. Hald, "Patch near–field acoustical holography using a new statistically optimal method," in *Proceedings of Inter-Noise 2003*, Seogwipo, Korea (August, 2003), pp. 2203–2210.
[5] J. Hald, "Basic theory and properties of statistically optimized near-field acoustical holography," J. Acoust. Soc. Am. **125**(4), 2105–2120 (2009).
[6] Y. T. Cho, J. S. Bolton, and J. Hald, "Source visualization by using statistically optimized nearfield acoustical holography in cylindrical coordinates," J. Acoust. Soc. Am. **118**(4), 2355–2364 (2005).
[7] Z. Wang and S. F. Wu, "Helmholtz equation-least-squares method for reconstructing the acoustic pressure field," J. Acoust. Soc. Am. **102**(4), 2020–2032 (1997).
[8] S. F. Wu, "On reconstruction of acoustic fields using the Helmholtz equation-least-squares method," J. Acoust. Soc. Am. **107**(5), 2511–2522 (2000).
[9] G. H. Koopmann, L. Song, and J. B. Fahnline, "A method for computing acoustic fields based on the principle of wave superposition," J. Acoust. Soc. Am. **86**(5), 2433–2438 (1989).
[10] L. Song, G. H. Koopmann, and J. B. Fahnline, "Numerical errors associated with the method of superposition for computing acoustic fields," J. Acoust. Soc. Am. **89**(6), 2625–2633 (1991).
[11] C. X. Bi, X. Z. Chen, J. Chen, and R. Zhou, "Nearfield acoustic holography based on the equivalent source method," Sci. China, Ser. E: Technol. Sci. **48**(3), 338–353 (2005).
[12] N. P. Valdivia and E. G. Williams, "Study on the comparison of the methods of equivalent sources and boundary element methods for near-field acoustic holography," J. Acoust. Soc. Am. **120**(6), 3694–3705 (2006).
[13] A. Sarkissian, "Extension of measurement surface in near-field acoustic holography," J. Acoust. Soc. Am. **115**(4), 1593–1596 (2004).
[14] A. Sarkissian, "Method of superposition applied to patch near-field acoustic holography," J. Acoust. Soc. Am. **118**(2), 671–678 (2005).
[15] S. F. Wu, H. Lu, and M. S. Bajwa, "Reconstruction of transient acoustic radiation from a sphere," J. Acoust. Soc. Am. **117**(4), 2065–2077 (2004).
[16] X.-Z. Zhang, C.-X. Bi, Y.-B. Zhang, and L. Xu, "Transient nearfield acoustic holography based on an interpolated time-domain equivalent source method," J. Acoust. Soc. Am. **130**(3), 1430–1440 (2011).
[17] J. Hald, "Time domain acoustical holography and its applications," Sound Vib. **35**, 16–24 (2001).
[18] J.-H. Thomas, V. Grulier, S. Paillasseur, J.-C. Pascal, and J.-C. Le Roux, "Real-time near-field acoustic holography for continuously visualizing nonstationary acoustic fields," J. Acoust. Soc. Am. **128**(6), 3554–3567 (2010).
[19] S. Paillasseur, J.-H. Thomas, and J.-C. Pascal, "Regularization for improving the deconvolution in real-time near-field acoustic holography," J. Acoust. Soc. Am. **129**(6), 3777–3787 (2011).
[20] M. Forbes, S. Letcher, and P. Stepanishen, "A wave vector, time-domain method of forward projecting time-dependent pressure fields," J. Acoust. Soc. Am. **90**(5), 2782–2792 (1991).
[21] V. Grulier, S. Paillasseur, J.-H. Thomas, J.-C. Pascal, and J.-C. Le Roux, "Forward propagation of time evolving acoustic pressure: Formulation and investigation of the impulse response in time-wavenumber domain," J. Acoust. Soc. Am. **126**(5), 2367–2378 (2009).
[22] Q. Leclere, "Acoustic imaging using under-determined inverse approaches: Frequency limitations and optimal regularization," J. Sound. Vib. **321**, 605–619 (2009).
[23] A. Tikhonov, "Solutions of incorrectly formulated problems and the regularization method," Sov. Math. Dokl. **4**, 1035–1038 (1963).
[24] P. C. Hansen, *Rank-Deficient and Discrete Ill-Posed Problems* (SIAM, Philadelphia, 1998), pp. 1–247.